

Large-scale simulations of vortex Majorana zero modes in topological crystalline insulators

Chun Yu Wan¹, Yujun Zhao¹, Yaoyi Li^{2,3,4}, Jinfeng Jia^{2,3,4,5,6},
Junwei Liu^{1*}

¹Department of Physics, Hong Kong University of Science and Technology, Clear Water Bay, Hong Kong, China.

²Key Laboratory of Artificial Structures and Quantum Control (Ministry of Education), Tsung-Dao Lee Institute, School of Physics and Astronomy, Shanghai Jiao Tong University, Shanghai, 200240, China.

³Hefei National Laboratory, Hefei, 230088, China.

⁴Shanghai Research Center for Quantum Sciences, Shanghai, 201315, China.

⁵Southern University of Science and Technology, Shenzhen, 518055, China.

⁶Quantum Science Center of Guangdong-Hong Kong-Macao Greater Bay Area (Guangdong), Shenzhen, 518045, China.

*Corresponding author(s). E-mail(s): liuj@ust.hk;

Abstract

Topological crystalline insulators are known to support multiple Majorana zero modes (MZMs) at a single vortex, their hybridization is forbidden by a magnetic mirror symmetry \mathbf{M}_T . Due to the limited energy resolution of scanning tunneling microscopes and the very small energy spacing of trivial bound states, it remains challenging to directly probe and demonstrate the existence of multiple MZMs. In this work, we propose to demonstrate the existence of MZMs by studying the hybridization of multiple MZMs in a symmetry breaking field. The different responses of trivial bound states and MZMs can be inferred from their spatial distribution in the vortex. However, the theoretical simulations are very demanding since it requires an extremely large system in real space. By utilizing the kernel polynomial method, we can efficiently simulate large lattices with over 10^8 orbitals to compute the local density of states which bridges the gap between theoretical studies based on minimal models and experimental measurements. We show that the spatial distribution of MZMs and trivial vortex bound states

indeed differs drastically in tilted magnetic fields. The zero-bias peak elongates when the magnetic field preserves M_T , while it splits when M_T is broken, giving rise to an anisotropic magnetic response. Since the bulk of SnTe are metallic, we also study the robustness of MZMs against the bulk states, and clarify when can the MZMs produce a pronounced anisotropic magnetic response.

Keywords: Majorana zero mode, Topological crystalline insulator, Topological phase transition, Vortex bound state

1 Introduction

Coupling MZMs in a controllable way is necessary for realizing fusion or braiding operations in topological quantum computation [1–7]. Most topological superconductors realized in experiments [8–21] only feature one MZM at each end, the MZMs from different ends can be coupled via junctions and/or gating [22–24]. However, some proposed designs are difficult to implement since the electric field may be screened by the superconducting substrate [25]. Alternatively, it is theorized that multiple MZMs can be realized in a single vortex in topological crystalline insulators [26, 27], the hybridization between MZMs at each end is prohibited by a magnetic mirror symmetry M_T . The coupling between MZMs can be controlled by an external field that breaks M_T [26]. In particular, the topological crystalline insulator SnTe [16, 28–32] is a promising platform since its superconductivity has been realized by proximity effect [33–38] and doping [39–51]. Although this magnetic mirror symmetry protection is first proposed in semiconductor nanowires with proximity-induced superconductivity [52], the topological phase with two MZMs is only stable at some fine-tuned range of parameters [53], and has not been identified experimentally.

However, the existence of crystal-symmetry-protected MZMs cannot be directly probed in experiments, the MZMs are obscured by low-lying vortex bound states [54]. And vortices in pristine SnTe could be close to a vortex phase transition [55, 56] as the bulk states are not gapped [29], MZMs from opposite surfaces may diffuse into the bulk and hybridize. The energy spacing of vortex bound states is approximately Δ_0^2/E_F [57–59], where Δ_0 is the superconducting gap at zero field and E_F is the Fermi energy. This energy spacing is about 10 μeV for conventional superconductors [54], which cannot be resolved in experiments, the observed zero-bias peaks (ZBPs) are usually due to non-zero energy vortex bound states [60]. Nevertheless, in the scanning tunneling microscopy and spectroscopy (STM/STS) study of topological insulator/-superconductor heterostructure $\text{Bi}_2\text{Te}_3/\text{NbSe}_2$, Xu et al. observed the local density of states (LDOS) changes from a V shape to a Y shape as the chemical potential decreases for samples with increasing thickness [11], consistent with the emergence of an MZM in the vortex phase transition [61, 62]. However, most previous theories of vortex MZMs omitted the bulk states [22, 27] or uses a small lattice that cannot simulate the spatial dependence of the MZMs and the trivial vortex bound states [26, 55, 56, 63–65].

We also study how the crystal-symmetry-protected MZMs in the SnTe material class are affected by the bulk states in vortex phase transitions. Previous theories

conclude the existence of two MZMs in a vortex in SnTe mainly by analysing the topological surface states with small external fields [26, 27]. Although MZMs can still exist in the presence of metallic bulk states up to a critical chemical potential $\mu = \mu_c$ at which a vortex phase transition occurs [26, 55, 56, 63–66], when the MZMs from opposite surfaces penetrate the bulk and annihilate, the number of MZMs may change as $2 \rightarrow 1 \rightarrow 0$ if there is no symmetry that guarantees the degeneracy of vortex line states [64]. This is because the symmetry M_T effectively promotes the vortex in SnTe to the Altland-Zirnbauer class BDI with the number of MZMs classified by \mathbb{Z} [26, 52, 64], in contrast to \mathbb{Z}_2 for 1D topological superconductors in class D [67, 68].

In this paper, we study response of the crystal-symmetry-protected MZMs in SnTe class materials in tilted magnetic fields, we simulate the LDOS and study the competition between MZMs and bulk states using kernel polynomial methods (KPM) [69, 70]. This method allows the simulation of Hamiltonian with dimension larger than 10^8 , bridging the gap between theoretical studies based on minimal models and experimental measurements. For a vortex in superconducting SnTe, we find that the ZBP strongly depends on the direction of the tilted magnetic field. For Fermi level close to the Dirac points, the ZBP elongates when the in-plane component of the field B_{\parallel} is along [110] preserving M_T , but it splits when B_{\parallel} is along [100] breaking M_T . At low chemical potential when all MZMs are hybridized, the ZBP splits for both directions. As the spatial distribution of the MZMs differs drastically under tilted magnetic fields, the anisotropic magnetic response can demonstrate the existence of symmetry-protected MZMs in experiments [71].

And we study the vortex phase transitions and evaluate the number of MZMs in tilted magnetic fields. We confirm that in an out-of-plane magnetic field, the number of MZMs changes as $0 \rightarrow 2$ as the chemical potential increases, in agreement with ref. 26. And we point out the single MZM phase is prohibited by a magnetic glide symmetry G_T and the particle-hole symmetry C . We then study the topological phase diagram in a tilted magnetic field which may break M_T and/or G_T and changes the classification of the vortex.

2 Kernel polynomial method

Previous studies simulate the LDOS of vortex states by expanding the radial part of the Bogoliubov quasiparticle amplitudes in Bessel series [62, 72, 73]. However, the efficiency relies on the cylindrical symmetry of the vortex states. Since a tilted magnetic field breaks the cylindrical symmetry and couples bases with different angular momenta, limiting the applicability of this numerical method. In this study we use KPM [69, 70] to compute the LDOS. Instead of calculating LDOS from the eigenstates and eigenenergies, we directly compute the LDOS in KPM by expanding the Green's functions in Chebyshev moments.

The retarded Green's function is given by [74]

$$G^R(E) = \frac{1}{E - H + i\eta}, \quad (1)$$

which can also be represented by the eigenenergies E_k and the eigenstates $|k\rangle$,

$$G^R(E) = \sum_k \frac{|k\rangle\langle k|}{E - E_k + i\eta}. \quad (2)$$

The LDOS for the i^{th} basis is defined as

$$d^i(E) = \sum_k \langle i|k\rangle\langle k|i\rangle\delta(E - E_k), \quad (3)$$

in the following sections the LDOS is summed over different spins and orbitals, we omit the summation below to simplify the notations. Comparing with eq. 2 we have

$$d^i(E) = -\frac{1}{\pi} \langle i|\text{Im}(G^R)|i\rangle. \quad (4)$$

where the Dirac delta function is replaced by a Lorentz function. And the imaginary part of the energy η determines the spectral width of the LDOS.

In KPM, the Green's functions are expanded in terms of Chebyshev moments, in this paper we focus on the diagonal parts which are the LDOS. First, since Chebyshev polynomials are defined in the range $[-1, 1]$, the Hamiltonian and the energy are rescaled by the maximum energy E_{max} , $\tilde{H} = H/E_{\text{max}}$ and $\tilde{E} = E/E_{\text{max}}$. We want to expand the LDOS in terms of Chebyshev moments, which are defined as

$$\mu_n^i = \int_{-1}^1 d^i(\tilde{E}) T_n(\tilde{E}) d\tilde{E}, \quad (5)$$

where $T_n(\tilde{E})$ is the n^{th} Chebyshev polynomial. Using eq. 1, we have

$$\mu_n^i = \langle i|T_n(\tilde{H})|i\rangle. \quad (6)$$

This moment is calculated recursively using

$$T_{n+1}(\tilde{H})|i\rangle = 2\tilde{H}T_n(\tilde{H})|i\rangle - T_{n-1}(\tilde{H})|i\rangle. \quad (7)$$

Finally, the LDOS is reconstructed using the moments μ_n^i and the kernel polynomials g_n which dampens the Gibbs oscillations of the partial sum.

$$d^i(\tilde{E}) \approx \frac{1}{\pi\sqrt{1-\tilde{E}^2}} \left[g_0\mu_0^i + 2 \sum_{n=1}^N g_n\mu_n^i T_n(\tilde{E}) \right]. \quad (8)$$

And we use the Jackson kernels

$$g_n = \frac{1}{N+1} \left[(N-n+1)\cos\left(\frac{\pi n}{N+1}\right) + \sin\left(\frac{\pi n}{N+1}\right)\cot\left(\frac{\pi}{N+1}\right) \right], \quad (9)$$

the spectral density has a Gaussian widening with width $\sigma \approx \frac{\pi E_{\max}}{N}$ [69]. For all KPM calculations in this work, $E_{\max} \approx 5$.

In experiments the resolution is lower than the energy spacing between the vortex bound states, which means a smaller number of moments N and reduces the computation time. Although KPM has been used to study vortex bound states [75–79], the systems in these studies are two-dimensional while we need to consider a three-dimensional system to account for the competition between the surface states and the bulk states, the dimension of the Hamiltonian is larger by two orders of magnitude.

3 Model Hamiltonian

Here we adopt a tight-binding model consisting of 3 p -orbitals for Sn (or Pb) and Te atoms respectively [28, 80, 81]. Our analysis is specific to the (001) surface of SnTe material class which have a rocksalt structure with valence band maximum (or conduction band minimum for PbTe) at L points [28, 30]. In real space, the Hamiltonian reads

$$\begin{aligned}
h = & \sum_j (m_j - \mu) \sum_{\mathbf{r}, s} \mathbf{c}_{js}^\dagger(\mathbf{r}) \cdot \mathbf{c}_{js}(\mathbf{r}) \\
& + \sum_{j, j'} t_{j, j'} \sum_{(\mathbf{r}, \mathbf{r}'), s} \left[\mathbf{c}_{js}^\dagger(\mathbf{r}) \cdot \mathbf{d}_{\mathbf{r}, \mathbf{r}'} \mathbf{d}_{\mathbf{r}, \mathbf{r}'} \cdot \mathbf{c}_{j's}(\mathbf{r}') + \text{H.c.} \right] \\
& + \sum_j i\lambda_j \sum_{\mathbf{r}, s, s'} \mathbf{c}_{js}^\dagger(\mathbf{r}) \times \mathbf{c}_{js'}(\mathbf{r}) \cdot \boldsymbol{\sigma}_{s, s'},
\end{aligned} \tag{10}$$

where $j = a, c$ represents the anion (Te) and the cation (Sn or Pb) respectively. The creation and annihilation operators $\mathbf{c}_{js}^\dagger(\mathbf{r}), \mathbf{c}_{js}(\mathbf{r})$ compose of the orbitals p_x, p_y and p_z . $\mathbf{d}_{\mathbf{r}, \mathbf{r}'}$ represents a unit vector between nearest neighbors $(\mathbf{r}, \mathbf{r}')$. λ_j is the atomic spin-orbit coupling strength. $\boldsymbol{\sigma}$ are the Pauli matrices for the spin basis. μ represents the chemical potential. We choose the parameters $m_c = -m_a = 1.65, t_{ac} = t_{ca} = 1.2$ and $l_a = l_c = 0.5$. The band structure for the (001) surface is plotted in Fig. 1(a), with $t_{cc} = -t_{aa} = 0.38$, the system is topologically nontrivial with Dirac cones protected by mirror symmetries M_{110} and $M_{1\bar{1}0}$ as in SnTe. For $t_{cc} = -t_{aa} = 0.33$, the system is gapped [Fig. 1(b)], this serves as a model for PbTe which is a trivial insulator. For the SnTe model, the Dirac points are at $E_D = -0.04$, and we consider the chemical potential starting from the Dirac points, denote as $\mu - E_D$, with $\mu - E_D < 0$ since SnTe is a p-type semiconductor. The (001) surface Brillouin zone for SnTe is shown in Fig. 1(c), there are four Dirac cones near the \bar{X} points. We consider superconductivity in SnTe with a single-gap s -wave pair potential, and omit the smaller gap related to the topological surface states [37, 48] to simplify the calculations. We include a superconducting vortex along the z direction,

$$\Delta(\rho, \theta) = \Delta_0 \tanh(\rho/\xi_0) e^{i\theta}, \tag{11}$$

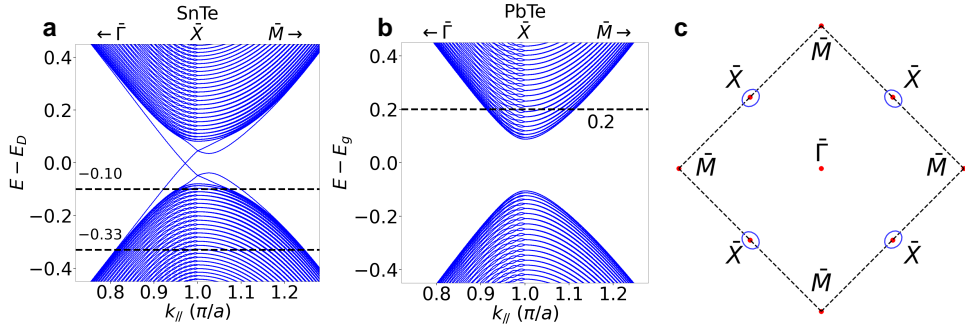


Fig. 1 (001) surface band structures for SnTe (a) and PbTe (b), $E_D = -0.04$ denotes the energy of the Dirac points. In our model for SnTe, the valence band maximum is at $E - E_D = -0.08$. The black dashed lines mark the chemical potential we use to simulate the LDOS. (c) Schematic diagram for the Fermi surface for the (001) surface Brillouin zone.

where $\rho = \sqrt{x^2 + y^2}$, $\theta = \tan^{-1}(y/x)$, Δ_0 is the superconducting gap and ξ_0 is the vortex core size. MZMs (if they exist) appear at the end points on the (001) and (00 $\bar{1}$) surfaces.

We consider an additional in-plane magnetic field B_{\parallel} in the form of a uniform Zeeman term (eq. 12) and keep the vortex profile unchanged to retain the translational symmetry in the z direction, this simplifies the calculations for the vortex phase transitions in Sec. 5. In experiments, the Zeeman term is mainly contributed by the orbital effect which has the same form as the spin effect for topological surface states [82, 83]. This approximation neglects the tilting of the vortex line, it is valid for a range below the surface of SnTe that is much shorter than the penetration depth of the superconducting substrate.

$$h_{\text{Zeeman}} = E_Z \sum_{j, \mathbf{r}, s, s'} \hat{\mathbf{B}}_{\parallel} \cdot \boldsymbol{\sigma}_{ss'} c_{js}^{\dagger}(\mathbf{r}) \cdot c_{js}(\mathbf{r}), \quad (12)$$

where E_Z is the Zeeman energy and $\boldsymbol{\sigma}$ are the Pauli matrices. In this paper we mainly consider the in-plane component of the magnetic field to be along [110] or [100] direction.

In experiments, identification of vortex MZMs is difficult because the energy levels are too closely packed. In the simulations this can be quantified by Δ_0/δ , where δ is the energy of the lowest vortex bound states other than the MZMs. Conventional superconductors have $\Delta_0/\delta \gg 1$, then the energy spacing is approximately equal [57–59], $E \approx n\delta$, where n is an integer. And δ depends on the Fermi energy and the vortex core size [57].

$$\delta \approx \frac{\Delta_0}{k_F \xi_0}, \quad (13)$$

where k_F is the Fermi wavevector. Since the vortex core size is proportional to the BCS coherence length in most superconductors, $\delta \sim \Delta_0^2/E_F$ [57] as mentioned in the introduction. In the simulations, we treat Δ_0 , ξ_0 and E_F as independent parameters, and $E_F = \mu - E_D$ for the topological surface states of SnTe. To simulate the LDOS

for the vortex bound states, the dimensionless quantity $\Delta_0/\delta \approx k_F\xi_0$ should be large so that the energy spectrum appears continuous as in experiments. Because the LDOS for the vortex bound states should vanish at the boundaries, the lattice must be large, with $N_x \gg \xi_0$ and $N_y \gg \xi_0$.

4 Local density of states

We choose lattices with $300 \times 300 \times 50$ atoms and $\xi_0 = 40$, the Hamiltonian has dimension $D \sim 10^8$ which is difficult to be diagonalized. The time complexity of KPM scales as $O(DN)$ [69, 70]. In KPM, the Green's functions are expanded as a partial sum involving N Chebyshev moments, and the energy resolution of the LDOS scales as E_{\max}/N for the Jackson kernel [69]. Since the energy resolution is inversely proportional to the number of iterations ($N/2$), we choose $\Delta_0 = 0.05$ to reduce computation time. Although Δ_0 is comparable to E_F , and makes the LDOS strongly asymmetric about E_F , we symmetrize it above and below E_F . For tilted magnetic fields, we choose the scanning direction of the LDOS along B_{\parallel} . For LDOS along either [110] or [100], only the Te atoms are sampled since the focus is on the valence bands.

The quality of the simulations can be checked by examining the ratio Δ_0/δ which can be approximated by $k_F\xi_0$. For $\mu - E_D = -0.1$, we have $\Delta_0/\delta = 8.22$ [Fig. 2(d)]. Although it is smaller than $k_F\xi_0 \sim 100$ for SnTe/Pb in the recent experiment [71], the LDOS has a Y shape [Fig. 2(a)] for $N = 2000$ when the individual vortex bound states cannot be resolved, these parameters qualitatively reproduce the LDOS in experiments.

4.1 Anisotropic magnetic response

For closely packed energy levels with $\Delta_0/\delta \gg 1$, the splitting of the ZBP strongly depends on the direction of B_{\parallel} and whether it preserves M_T , we call this the anisotropic magnetic response of the vortex bound states. For $E_Z = 0.4\Delta_0$, the anisotropic magnetic response is apparent even at $N = 2000$. For B_{\parallel} along [100] which destroys M_T that protects the MZMs, the ZBP moves towards the opposite direction of B_{\parallel} , the splitting enlarges and the LDOS resembles a V shape [Fig. 2(b)]. For B_{\parallel} along [110], $M_T = TM_{1\bar{1}0}$ is preserved, the ZBP elongates and does not split even away from the vortex core [Fig. 2(c)].

Using $N = 20000$, we can resolve the energy spacing between some vortex bound states [Fig. 2(d-f)]. In particular, for B_{\parallel} along [110], we can see that the extended ZBP from Fig. 2(f) consists of vortex bound states other than the MZMs. This anisotropic magnetic response originates from the nontrivial spin texture of the topological surface states in SnTe, it is not a direct consequence of destroying or preserving the MZMs. Further increasing the resolution to $N = 70000$ at the sites with the highest LDOS, we confirm that the MZMs are hybridized when B_{\parallel} is along [100]. The anisotropic magnetic response is pronounced even at low resolution when the splitting of the MZMs cannot be observed, in Fig. 2(h), the splitting is only 0.90% of the superconducting gap Δ_0 for Zeeman energy $E_Z = 0.4\Delta_0$.

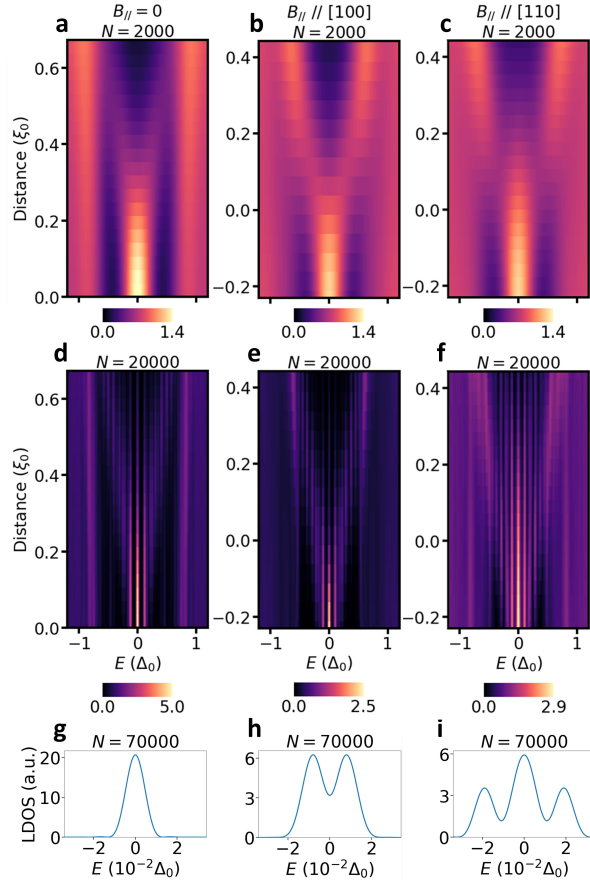


Fig. 2 Vortex LDOS for the (001) surface of SnTe in tilted magnetic fields at different resolutions. MZMs are hybridized in the second column when B_{\parallel} is along [100] breaking M_T . The resolution is enhanced by increasing the number of Chebyshev moments N in KPM. (a-c) $N = 2000$ where the individual vortex bound states are not resolved, the ZBP is sensitive to the direction of B_{\parallel} . (d-f) LDOS for $N = 20000$ and the vortex bound states are resolved. (g-i) LDOS for $N = 70000$ at the density peaks, MZMs are absent in (h). The Zeeman energy is $E_Z = 0.4\Delta_0$ and $\Delta_0 = 0.05$.

4.2 Comparisons with trivial phases

As studied in Sec. 5, the MZMs can be hybridized at low chemical potential $\mu < \mu_c$ in vortex phase transitions without breaking any symmetry, and we find that the magnetic response becomes isotropic at lower μ when the LDOS is dominated by bulk states. For SnTe at $\mu - E_D = -0.10$, the anisotropic magnetic response [Fig. 3(a,d)] arises because the vortex bound states are mostly contributed by the topological surface states which are sensitive to the direction of B_{\parallel} . At $\mu - E_D = -0.33$, the MZMs diffuse into the bulk and hybridize (confirmed with KPM in Appendix A), the LDOS on the surface is mostly contributed by the bulk bands, the splitting of the ZBP becomes isotropic [Fig. 3(b,e)]. In Appendix A, we also show the LDOS at fixed E_Z

and various μ . The change in the magnetic response of the LDOS is gradual and not sensitive to the number of MZMs (Fig. A2).

We further confirm the isotropic magnetic response arises from the bulk states by comparing with PbTe which does not feature topological surface states. The ZBP splits for either directions of B_{\parallel} [Fig. 3(c,f)]. Although in Fig. 3(e,f) there are states at distance > 0 similar to the elongated ZBP in 3(d), their density is weak and the LDOS still has a V shape, the slight anisotropy in the trivial cases could be caused by the underlying cubic lattice.

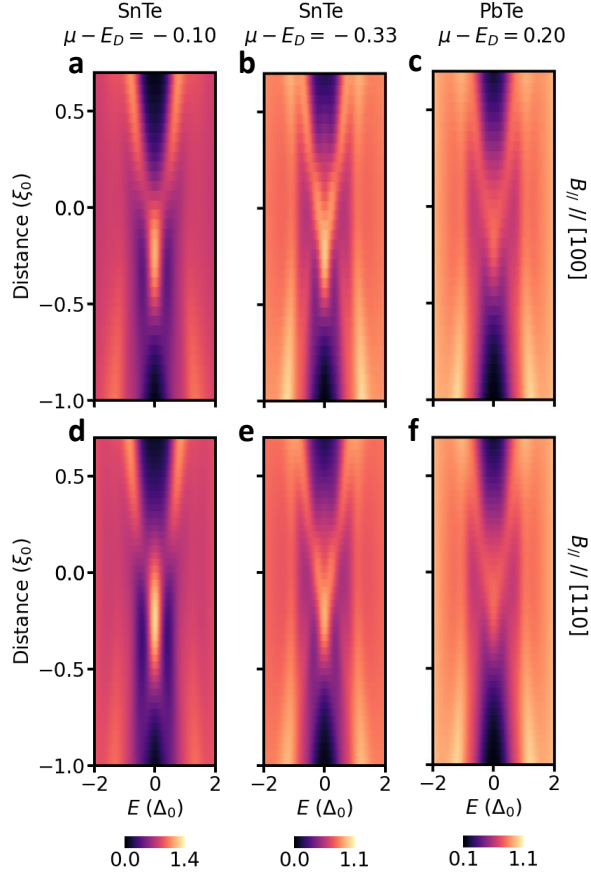


Fig. 3 Vortex LDOS in tilted magnetic field for SnTe and PbTe. (a-c) When B_{\parallel} is along [100], any mirror-symmetry-protected MZMs must be hybridized, and the ZBPs split. (d-f) When B_{\parallel} is along [110], M_T is preserved and SnTe at low chemical potential supports two MZMs. For SnTe in the topological phase, the ZBP extends much longer than SnTe at low chemical potential as the MZMs diffusive into the bulk and may hybridize. $E_Z = 0.4\Delta_0$ for (a, d), and $E_Z = 0.3\Delta_0$ for the other subplots.

5 Vortex Phase Transitions

5.1 Under out-of-plane magnetic field

We construct the Bogoliubov-de Gennes (BdG) Hamiltonian for the vortex line (eq. 14) which is periodic in the z direction, and we define the symmetry operators in Appendix B.

$$H_{\text{BdG}}(k_z) = \begin{pmatrix} h(k_z) & \Delta(\rho, \theta)i\sigma_y \\ -\Delta^*(\rho, \theta)i\sigma_y & -h^T(-k_z) \end{pmatrix}, \quad (14)$$

where $\Delta(\rho, \theta) = \Delta_0 \tanh(\rho/\xi_0) e^{i\theta}$.

We clarify the number of MZMs in SnTe which features four Dirac cones protected by M_{110} and $M_{\bar{1}\bar{1}0}$. Since a superconducting vortex breaks mirror symmetries, the system preserves magnetic mirror symmetries M_T instead. Although either magnetic mirror symmetry $M_T = M_{110}T$ or $M_{\bar{1}\bar{1}0}T$ can protect two MZMs, in an out-of-plane magnetic field when the system preserves both, it still hosts only two MZMs. As the system respects a screw symmetry S_{4z} , the Hamiltonian can be block-diagonalized by S_{4z} with eigenvalues $\{1, i, -1, -i\}$ [65, 84]. Since the particle-hole symmetry C exchanges the i and $-i$ blocks, only the 1 and -1 blocks can support MZMs which are self-Hermitian. Since M_T commutes with S_{4z} , there is chiral symmetry within each block, these two blocks can each support multiple MZMs [64]. Although this model for SnTe with S_{4z} symmetry is classified by $\mathbb{Z} \times \mathbb{Z}$, we only find two MZMs with our range of parameters. Our conclusions are consistent with refs. 26, 27 that evaluate the number of MZMs using the Jackiw-Rossi model [85] for the multiple Dirac cones in SnTe.

A vortex phase transition is signaled by (1) a crossing of the bulk energy, (2) appearance or disappearance of boundary states and (3) a change in the topological invariant. In Fig. 4(a, d-g), we show the vortex line energy as a function of chemical potential μ . As μ increases, the Fermi level is closer to the Dirac points and there are two sets of crossings, $\mu_c = -0.242, -0.236$. We use recursive Green's functions [86] to calculate the number of zero energy states and show their distribution near the surface (Appendix C). The system respects a chiral symmetry ($\Gamma = CM_T$, the explicit form is given in Appendix B and a winding number ν can be defined (Appendix D), and it corresponds to the number of MZMs at each end of the vortex line [52, 64]. We label the vortex line energy with screw symmetry S_{4z} eigenvalues, the MZMs have eigenvalues ± 1 and they hybridize at the first crossing point [Fig. 4(e)]. The remaining crossings have eigenvalues $\pm i$ [Fig. 4(f)] and they do not couple to the MZMs. Since the crossings for eigenvalues $\pm i$ occurs at $k_z = \pi/a$ and they overlap, the gap will open again and there are no nodal vortex phases in this model for $\mu - E_D < 0$.

Although ref. 26 shows that M_T can protect two MZMs by analyzing the surface Hamiltonian, it is possible that the number of MZMs changes as $2 \rightarrow 1 \rightarrow 0$ during the vortex phase transitions [64]. Then if we introduce a perturbation that breaks M_T , the system changes from the Altland-Zirnbauer class BDI to D which can still host a single MZM [52]. However, this is forbidden if a magnetic glide symmetry $G_T = TG_y$ or TG_x is present. As shown in Fig. 4(a-c), the vortex line energy is at least two-fold degenerate at $k_z = \pi/a$ since $G_T^2 = -1$ at that point. And the transition at k_z away from π/a must also appear in pairs because of the particle-hole symmetry C which

gives $CH(k_z)C^{-1} = -H(-k_z)$. The symmetries C , M_T and G_T together forbid an odd number of MZMs. For odd $N_x = N_y$, there is no G_T and a single MZM can be realized (Fig. E1). And S_{4z} is replaced by C_{4z} which does not exchange the sublattices. However, in experiments the vortex size is much larger than the lattice parameter so that there is no difference between even and odd $N_x = N_y$. The $\nu = 1$ phase for odd $N_x = N_y$ is an artifact from the small lattice used in the calculations.

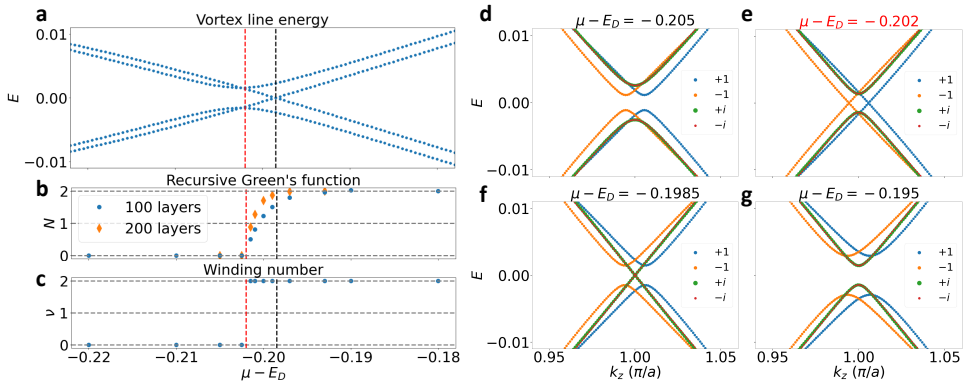


Fig. 4 Vortex phase transition in SnTe in an out-of-plane magnetic field. (a) The vortex line energy at $k_z = \pi/a$, it is at least two-fold degenerate due to G_T . The number of MZMs are calculated using recursive Green's functions (b) and winding number (c). The black dots denote crossings at $k_z = \pi/a$, the red dots are for $k_z \neq \pi/a$. (d-g) Vortex line energy for different k_z , the colors denote the S_{4z} eigenvalues. We use $\Delta_0 = 0.1$, $\xi_0 = 1$ for the vortex and $N_x = N_y = 20$ for the lattice.

5.2 Under tilted magnetic field

For B_{\parallel} along $[110]$, the system can still host two MZMs as $TM_{1\bar{1}0}$ is preserved. We determine the phase diagram for different μ and E_Z . Since both TG_x and TG_y are broken, the degeneracy at $k_z = \pi/a$ is lifted and the system can host a single MZM in between vortex phase transitions. Without S_{4z} , the number of MZMs ν changes at each crossing point. For $E_Z > 0.006$, all crossing points occur at $k_z = \pi/a$ with ν changes by 1 [Fig. 5(b-e)]. And the regions with $\nu = 1$ grows with increasing E_Z .

For B_{\parallel} along $[100]$, the system cannot host two MZMs as TM_{110} and $TM_{1\bar{1}0}$ are broken. Since TG_y is preserved, the vortex line energy is at least two-fold degenerate at $k_z = \pi/a$ [Fig. 5(f-i)]. TG_y and C ensure ν can only change by 2 in a vortex phase transition, because $\nu = 0$ or 2 at $E_Z = 0$, we have $\nu = 0$ for any μ and E_Z .

Even when M_T is preserved, the MZMs can be hybridized if $\mu < \mu_c$. From the vortex line energy and the winding number we conclude the number of MZMs to be $\nu \in \{0, 1, 2\}$ for B_{\parallel} along $[110]$, and $\nu = 0$ for B_{\parallel} along $[100]$. The conditions for the $\nu = 2$ phase we determined may allow schemes to braid the two MZMs in a single vortex by changing the direction of the magnetic field or other symmetry-breaking fields.

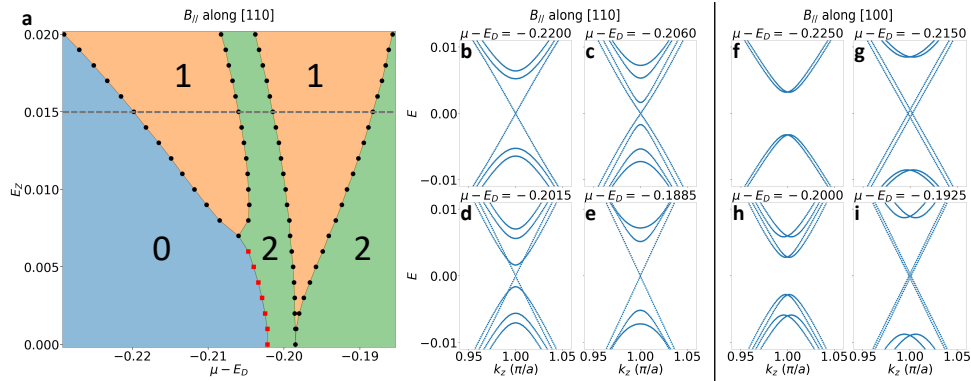


Fig. 5 Vortex phase transition in SnTe in tilted magnetic fields. We include the in-plane component as a Zeeman field and consider it along [110] and [100] directions. The phase diagram of vortex phase transition for B_{\parallel} along [110] at various chemical potential μ and Zeeman energy E_Z (a). The red dots denote a pair of crossings at $(k_z, 2\pi/a - k_z)$ for $k_z \neq \pi/a$ enforced by particle-hole symmetry. The four crossings at $E_Z = 0.015$ occur at $k_z = \pi/a$ (b-e). For comparison, TG_y is preserved when B_{\parallel} is along [100], it ensures the energy at $k_z = \pi/a$ is at least two-fold degenerate (f-i).

Although we evaluated the number of MZMs in SnTe using a small lattice model, the LDOS in the last section is calculated using the same lattice model with larger N_x , N_y and ξ_0 , the conclusions for topology of the vortex still applies but the phase transition points (μ_c, E_{Zc}) may vary.

6 Conclusions

We have studied the topological vortex phases of topological crystalline insulator SnTe in tilted magnetic fields. We verified that two MZMs can coexist in a vortex protected by a magnetic mirror symmetry, and we pointed out that a single MZM in between vortex phase transitions is prohibited if a magnetic glide symmetry is preserved. By extending the calculations to larger lattice models, we found that the LDOS displays an anisotropic magnetic response when the vortex features MZMs. It is due to the drastic difference between the spatial distribution of MZMs and trivial vortex bound states. This anisotropic magnetic response remains robust for a range of μ below the valence band maximum and gradually disappears when MZMs diffuse into the bulk. The elongated ZBP in a tilted magnetic field that preserves M_T is a distinct experimental signature of the symmetry-protected MZMs in a vortex in a topological crystalline insulator.

Acknowledgements. The simulations were done on the Hefei advanced computing center and Tianhe-2 in the National Supercomputer Center in Guangzhou.

Funding. We acknowledge the financial support from the National Key R&D Program of China (Grants No. 2021YFA1401500), the National Science Foundation of China (Grants No. 12022416) and the Hong Kong Research Grants Council (Projects No. N_HKUST626/18, ECS26302118 and 16305019).

Author contribution. JL supervised the project. CYW and YZ performed the calculations. CYW, YZ, YL, JJ and JL analysed the results. JL and CYW wrote the manuscript with contributions from all authors.

Appendix A LDOS at various chemical potential

In this section we study how the magnetic response of the LDOS changes as μ is varied. Although we could not determine the precise topological phase diagram for $N_x = N_y = 300$ as we did for $N_x = N_y = 20$ in Figs. 4 and 5, we can confirm that Fig. 3(e) with $\mu - E_D = -0.33$ and $E_Z = 0.3\Delta_0$ does not feature MZMs by increasing the resolution of the LDOS calculated with the KPM. Similar to Fig. 2(g-i), we only choose the sites with the highest LDOS at $E = 0$ and $N = 2000$ for calculations with high resolution. In Fig. A1(a, c), there are no MZMs since the LDOS does not peak at $E = 0$. For B_{\parallel} along [100], as M_T is broken, the small peak at $E = 0$ does not imply existence of MZMs, it originates from bulk states with energy much lower than the resolution.

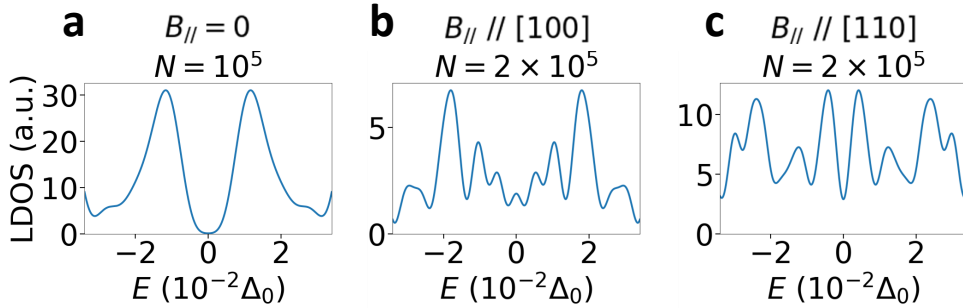


Fig. A1 LDOS at high resolution for $\mu - E_D = -0.33$. In vertical magnetic field (a), in tilted magnetic fields with B_{\parallel} along [100] (b), and along [110] (c). We choose the sites with the highest LDOS at $E = 0$ for $N = 2000$. For (b, c) the Zeeman energy is $E_Z = 0.3\Delta_0$.

In Fig. A2 we show the vortex LDOS with different E_F for B_{\parallel} along [100] and [110] with fixed Zeeman energy $E_Z = 0.4\Delta_0$. We define $E_F = \mu - E_D$ to shorten the notations in the figure. At $E_F = -0.33$ far below the Dirac points, the LDOS have a similar V-shape in either directions since they are due to the nearly isotropic bulk states. Since the vortex states are mainly contributed by bulk states that decay slowly beneath the surface, and the thickness of our lattice ($N_z = 50$) is comparable to the vortex size, the vortex LDOS on the top surface has contribution from the bottom surface which appears as an upside-down V shape in Fig. A2 (a, g). As E_F increases (closer to the Dirac points), the magnetic response becomes more anisotropic. The ZBP elongates for B_{\parallel} along [110] and deviates from the V shape when B_{\parallel} is along [100]. And the LDOS does not depend sensitively on the phase transition that destroy the MZMs, the change in the magnetic response originates from competition between the MZMs and the bulk states as explained in Sec. 4.2.

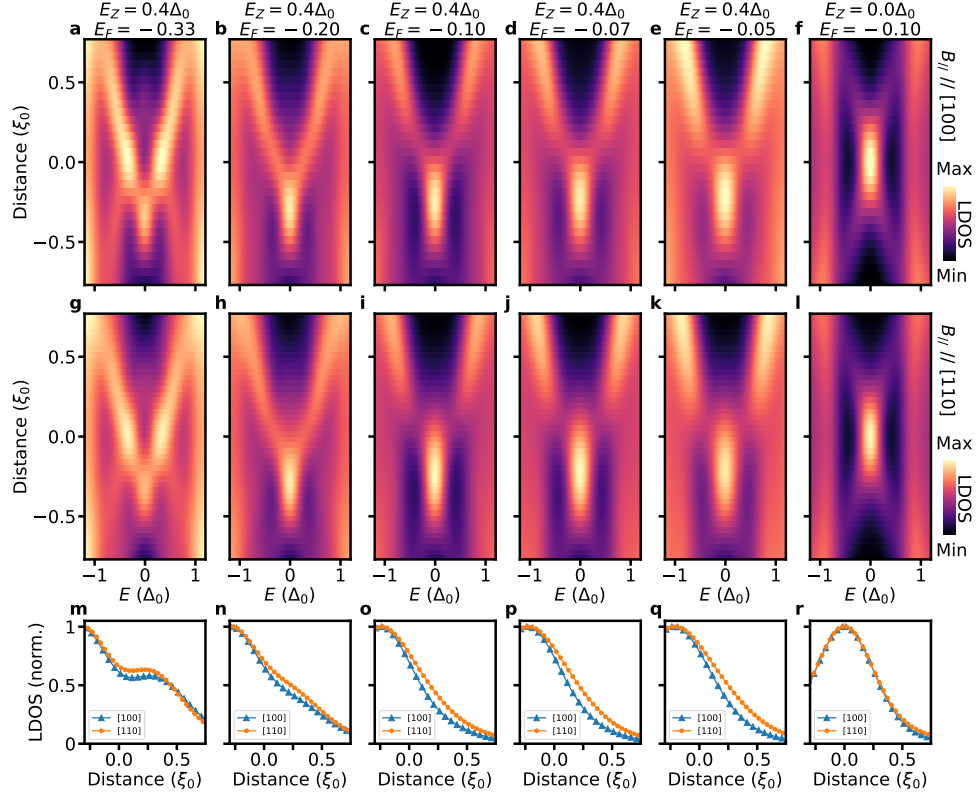


Fig. A2 Vortex LDOS for the (001) surface of SnTe in tilted magnetic fields at various Fermi energy E_F ($E_F = \mu - E_D$) and $E_Z = 0.4\Delta_0$. The number of moments is $N = 2000$. The bottom row shows the LDOS at $E = 0$ for either scanning direction which is also the direction of $B_{||}$. The rightmost column shows the LDOS in vertical magnetic field for comparisons, there is a slight anisotropy in the LDOS due to the square lattice (r). Other parameters are the same as in Fig. 2.

Appendix B Symmetry operators for the tight-binding model

The symmetry operators for the BdG Hamiltonian for a vortex line (eq. 2 in the main text) can be decomposed into 5 parts

$$O_{\text{vortex}} = O_{\text{ph}} \otimes O_{x,y} \otimes O_z \otimes O_{\text{orb}} \otimes O_{\text{spin}}. \quad (\text{B1})$$

O_{ph} is in the Nambu basis. $O_{x,y}$ and O_z are for the sites in the supercell for the vortex line, $z = 0, 1$ since there are 2 sublattices. O_{orb} is for orbitals p_x, p_y and p_z . O_{spin} is for the spin basis.

The particle-hole symmetry operator is

$$C_{\text{ph}} = \begin{pmatrix} 0 & K \\ K & 0 \end{pmatrix}, \quad (\text{B2})$$

where K is the complex conjugation operator. The Hamiltonian satisfies $CH_{\text{BdG}}(k_z)C^{-1} = -H_{\text{BdG}}(-k_z)$ with $C^2 = +1$.

The magnetic mirror symmetry $M_T = TM_{1\bar{1}0}$ is written as

$$M_T = \begin{pmatrix} e^{i\pi/4}i\sigma_y m_{1\bar{1}0}^* K & 0 \\ 0 & e^{-i\pi/4}i\sigma_y m_{1\bar{1}0} K \end{pmatrix}, \quad (\text{B3})$$

where σ_y is a Pauli matrix in the spin basis. The phase factors $e^{\pm i\pi/4}$ are introduced to cancel the phases generated when rotating the vortex [84]. And $m_{1\bar{1}0}$ is the mirror symmetry operator for the band Hamiltonian

$$m_{1\bar{1}0} = m_{1\bar{1}0}^{(xy)} \otimes \mathbb{I}_2 \otimes \begin{pmatrix} 0 & 1 & 0 \\ 1 & 0 & 0 \\ 0 & 0 & 1 \end{pmatrix} \otimes \frac{i}{\sqrt{2}} (\sigma_x + \sigma_y), \quad (\text{B4})$$

where $m_{1\bar{1}0}^{(xy)}$ transforms (x, y) to (y, x) and \mathbb{I}_2 is an identity in the z basis. And the origin $(0, 0)$ is the center of the lattice.

The Hamiltonian satisfies $M_T H_{\text{BdG}}(k_z) M_T^{-1} = H_{\text{BdG}}(-k_z)$ with $M_T^2 = +1$, it acts as an effective time-reversal symmetry. A chiral symmetry operator can be defined by $\Gamma = M_T C$, The Hamiltonian satisfies $\Gamma H_{\text{BdG}}(k_z) \Gamma^{-1} = -H_{\text{BdG}}(k_z)$ with $\Gamma^2 = +1$ [67, 68, 87]. In this case the 1D vortex line in SnTe belongs to Altland-Zirnbauer class BDI with a topological invariant of integer values [52, 67].

For even N_x and N_y , the system preserves nonsymmorphic symmetries that interchanges the sublattices [65]. The magnetic glide symmetry $G_T = TG_y$ is written as

$$G_T = \begin{pmatrix} i\sigma_y g_y^*(k_z) K & 0 \\ 0 & i\sigma_y g_y(-k_z) K \end{pmatrix}, \quad (\text{B5})$$

$$g_y = g_y^{(xy)} \otimes \begin{pmatrix} 0 & e^{-ik_z a/2} \\ e^{ik_z a/2} & 0 \end{pmatrix} \otimes \begin{pmatrix} 1 & 0 & 0 \\ 0 & -1 & 0 \\ 0 & 0 & 1 \end{pmatrix} \otimes (-i\sigma_y) \quad (\text{B6})$$

and $g_y^{(xy)}$ transforms (x, y) to $(x, -y)$. And $G_T^2 = -1$ at $k_z = -\pi/a$ guarantees a Kramers degeneracy for the vortex line.

And the screw symmetry operator S_{4z} is written as

$$S_{4z} = \begin{pmatrix} e^{i\pi/4} s_{4z}(k_z) & 0 \\ 0 & e^{-i\pi/4} s_{4z}^*(-k_z) K \end{pmatrix}, \quad (\text{B7})$$

$$s_{4z} = s_{4z}^{(xy)} \otimes \begin{pmatrix} 0 & e^{ik_z a/2} \\ e^{-ik_z a/2} & 0 \end{pmatrix} \otimes \begin{pmatrix} 0 & -1 & 0 \\ 1 & 0 & 0 \\ 0 & 0 & 1 \end{pmatrix} \otimes \frac{1}{\sqrt{2}}(\sigma_0 - i\sigma_z) \quad (\text{B8})$$

and $s_{4z}^{(xy)}$ transforms (x, y) to $(-y, x)$.

Appendix C Recursive Green's Functions

We use recursive Green's functions [86] to calculate the number of zero-energy states near the surface. The LDOS $d^i(E)$ is defined in Eq. 3 of the main text. We calculate the number of zero-energy states by integrating the LDOS using η smaller than the lowest nonzero eigenenergy. We checked that for our choice of parameters we can use $\eta = 10^{-6}$, and $d^i(E)$ can be described by a single Lorentz function.

$$d^i(E) \approx \frac{1}{\pi} \sum_{E_k=0} \langle i|k\rangle \langle k|i\rangle \frac{\eta}{(E - E_k)^2 + \eta^2}. \quad (\text{C9})$$

The energy integration can be replaced by $\pi\eta d^i(E=0)$.

Since the Hamiltonian has no z dependence, the surface Green's functions can be obtained recursively [86]. And we define the LDOS for each layer at zero energy as $D(z)$. We iterate the surface Green's functions to obtain the LDOS for n_z layers below the surface. Then the number of MZMs can be approximated by

$$N = \sum_{z=1}^{n_z} D(z), \quad (\text{C10})$$

the results are shown in Fig. 4(b) in the main text using $n_z = 100, 200$. In Fig. C1 we show $D(z)$ for some values of (μ, E_Z) . Near the phase transition points the MZMs penetrate too deep inside the bulk [61, 62], and N deviates from an integer value [e.g., Fig. 4(b) in the main text].

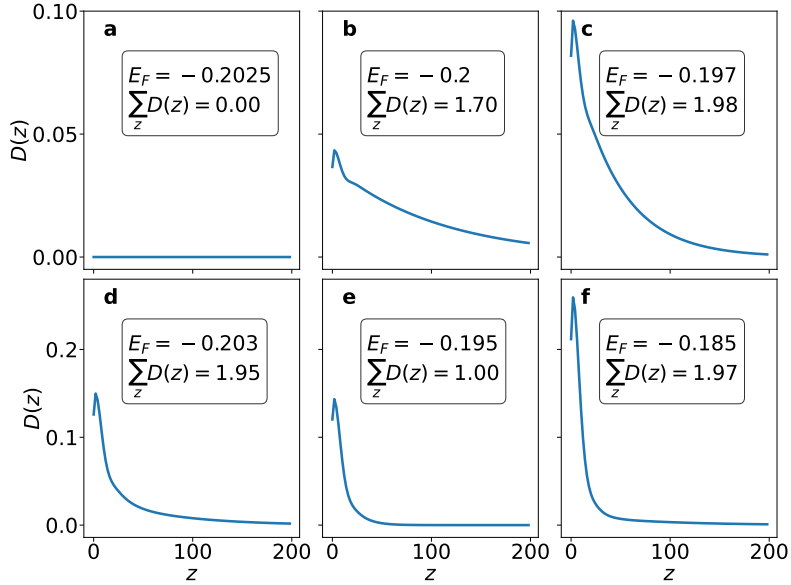


Fig. C1 Distribution of the MZMs $D(z)$ for the top $n_z = 200$ layers. Zeeman energy $E_Z = 0$ in (a-c) and $E_Z = 0.015$ in (d-f). $E_F = \mu - E_D$ as defined in the main text.

Appendix D Winding number

The number of MZMs is equal to the winding number

$$\nu = \frac{1}{2\pi} \int_0^{2\pi} d\theta(k_z), \quad (\text{D11})$$

where $\theta(k_z)$ is the angle of the \mathbf{d} vector in Nambu space. For a vortex line (eq. 2 in the main text) the winding number is generalized to include other degrees of freedom (sites, spins, orbitals, etc.), which is defined as [52, 64, 88]

$$\nu = \frac{1}{4\pi i} \int_0^{2\pi} dk_z \text{Tr} \left[\Gamma \frac{H_{BdG}(k_z)}{dk_z} H_{BdG}^{-1}(k_z) \right]. \quad (\text{D12})$$

We show the integrands for some values of (μ, E_Z) in Fig. D1. Previous references for vortex phase transitions only calculated the crossing of vortex line to deduce the change of the number of MZMs, which leads to ambiguous results when the system preserves a chiral symmetry that supports multiple MZMs. In Fig. D1 (d-f), we explicitly show that ν changes as $2 \rightarrow 1 \rightarrow 2$, and the result is consistent with the number of MZMs at each end obtained in the last section.

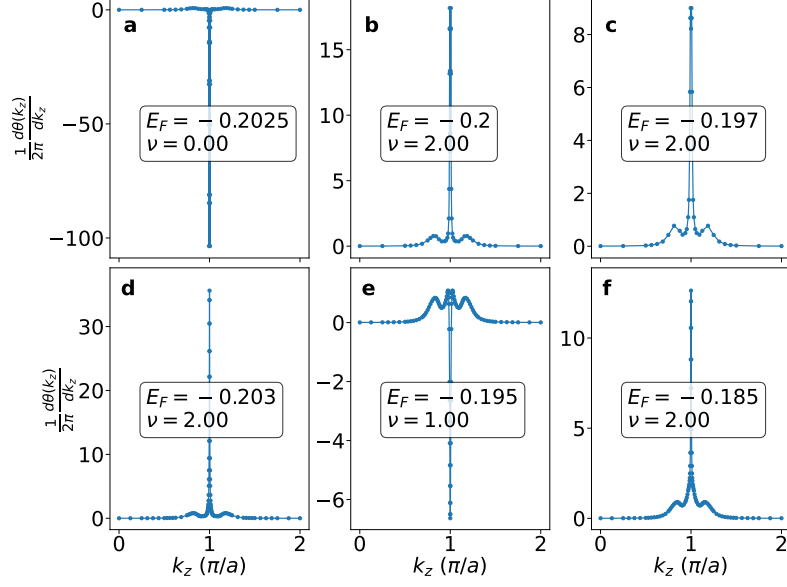


Fig. D1 The integrands of the winding number. Zeeman energy $E_Z = 0$ in (a-c) and $E_Z = 0.015$ in (d-f).

Appendix E Vortex phase transitions for odd $N_x = N_y$

In the main text we have shown that the single MZM phase may appear between vortex phase transitions if G_T is broken, and confirmed it using an in-plane Zeeman field that breaks G_T . In Fig. E1 we show $\nu = 1$ can also be realized in system with odd $N_x = N_y$ that breaks G_T . The calculations are the same as those for Fig. 4 in the main text, except that in Fig. E1 (d-g) we show the C_{4z} eigenvalues since S_{4z} is broken.

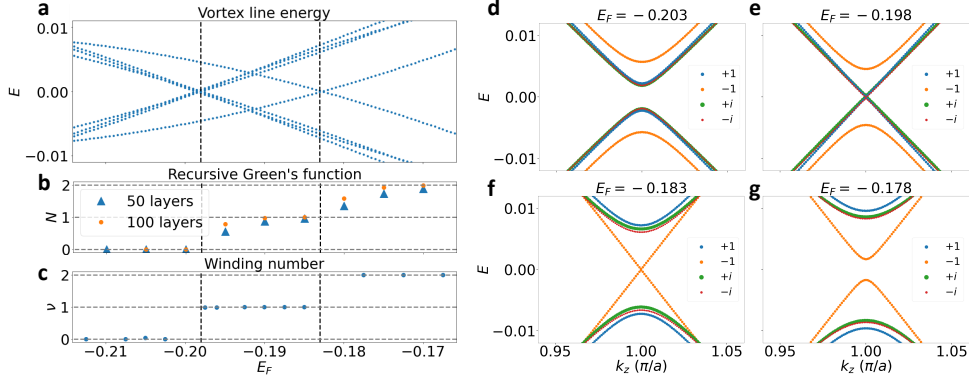


Fig. E1 Vortex phase transition in SnTe under an out-of-plane magnetic field. (a) The vortex line energy at $k_z = \pi/a$, it can be non-degenerate since G_T is broken. The number of MZMs are calculated using recursive Green's functions (b) and winding number (c). The black dashed lines denote crossings at $k_z = \pi/a$. (d-g) Vortex line energy for different k_z , the colors denote the C_{4z} eigenvalues. We use $\Delta_0 = 0.1$, $\xi_0 = 1$ for the vortex and $N_x = N_y = 21$ for the lattice.

References

- [1] Kitaev, A.Y.: Fault-tolerant quantum computation by anyons. *Annals of Physics* **303**(1), 2–30 (2003)
- [2] Alicea, J.: New directions in the pursuit of Majorana fermions in solid state systems. *Reports on Progress in Physics* **75**(7), 076501 (2012)
- [3] Sarma, S.D., Freedman, M., Nayak, C.: Majorana zero modes and topological quantum computation. *npj Quantum Information* **1**(1), 1–13 (2015)
- [4] Aasen, D., Hell, M., Mishmash, R.V., Higginbotham, A., Danon, J., Leijnse, M., Jespersen, T.S., Folk, J.A., Marcus, C.M., Flensberg, K., *et al.*: Milestones toward Majorana-based quantum computing. *Physical Review X* **6**(3), 031016 (2016)
- [5] Lutchyn, R.M., Bakkers, E.P., Kouwenhoven, L.P., Krogstrup, P., Marcus, C.M., Oreg, Y.: Majorana zero modes in superconductor–semiconductor heterostructures. *Nature Reviews Materials* **3**(5), 52–68 (2018)
- [6] Beenakker, C.: Search for non-Abelian Majorana braiding statistics in superconductors. *SciPost Physics Lecture Notes*, 015 (2020)
- [7] Awoga, O.A., Ioannidis, I., Mishra, A., Leijnse, M., Trif, M., Posske, T.: Controlling Majorana hybridization in magnetic chain-superconductor systems. *Physical Review Research* **6**(3), 033154 (2024)
- [8] Mourik, V., Zuo, K., Frolov, S.M., Plissard, S., Bakkers, E.P., Kouwenhoven,

- L.P.: Signatures of Majorana fermions in hybrid superconductor-semiconductor nanowire devices. *Science* **336**(6084), 1003–1007 (2012)
- [9] Das, A., Ronen, Y., Most, Y., Oreg, Y., Heiblum, M., Shtrikman, H.: Zero-bias peaks and splitting in an Al–InAs nanowire topological superconductor as a signature of Majorana fermions. *Nature Physics* **8**(12), 887–895 (2012)
- [10] Nadj-Perge, S., Drozdov, I.K., Li, J., Chen, H., Jeon, S., Seo, J., MacDonald, A.H., Bernevig, B.A., Yazdani, A.: Observation of Majorana fermions in ferromagnetic atomic chains on a superconductor. *Science* **346**(6209), 602–607 (2014)
- [11] Xu, J.-P., Wang, M.-X., Liu, Z.L., Ge, J.-F., Yang, X., Liu, C., Xu, Z.A., Guan, D., Gao, C.L., Qian, D., *et al.*: Experimental detection of a majorana mode in the core of a magnetic vortex inside a topological insulator-superconductor Bi₂Te₃/NbSe₂ heterostructure. *Physical Review Letters* **114**(1), 017001 (2015)
- [12] Yin, J.-X., Wu, Z., Wang, J., Ye, Z., Gong, J., Hou, X., Shan, L., Li, A., Liang, X., Wu, X., *et al.*: Observation of a robust zero-energy bound state in iron-based superconductor Fe(Te, Se). *Nature Physics* **11**(7), 543–546 (2015)
- [13] Ruby, M., Pientka, F., Peng, Y., Von Oppen, F., Heinrich, B.W., Franke, K.J.: End states and subgap structure in proximity-coupled chains of magnetic adatoms. *Physical Review Letters* **115**(19), 197204 (2015)
- [14] Ménard, G.C., Guissart, S., Brun, C., Leriche, R.T., Trif, M., Debontridder, F., Demaille, D., Roditchev, D., Simon, P., Cren, T.: Two-dimensional topological superconductivity in Pb/Co/Si (111). *Nature Communications* **8**(1), 1–7 (2017)
- [15] Zhang, P., Yaji, K., Hashimoto, T., Ota, Y., Kondo, T., Okazaki, K., Wang, Z., Wen, J., Gu, G., Ding, H., *et al.*: Observation of topological superconductivity on the surface of an iron-based superconductor. *Science* **360**(6385), 182–186 (2018)
- [16] Wang, D., Kong, L., Fan, P., Chen, H., Zhu, S., Liu, W., Cao, L., Sun, Y., Du, S., Schneeloch, J., *et al.*: Evidence for Majorana bound states in an iron-based superconductor. *Science* **362**(6412), 333–335 (2018)
- [17] Liu, Q., Chen, C., Zhang, T., Peng, R., Yan, Y.-J., Lou, X., Huang, Y.-L., Tian, J.-P., Dong, X.-L., Wang, G.-W., *et al.*: Robust and clean Majorana zero mode in the vortex core of high-temperature superconductor (Li_{0.84}Fe_{0.16})OHFeSe. *Physical Review X* **8**(4), 041056 (2018)
- [18] Machida, T., Sun, Y., Pyon, S., Takeda, S., Kohsaka, Y., Hanaguri, T., Sasagawa, T., Tamegai, T.: Zero-energy vortex bound state in the superconducting topological surface state of Fe(Se, Te). *Nature Materials* **18**(8), 811–815 (2019)
- [19] Manna, S., Wei, P., Xie, Y., Law, K.T., Lee, P.A., Moodera, J.S.: Signature of a pair of Majorana zero modes in superconducting gold surface states. *Proceedings*

of the National Academy of Sciences **117**(16), 8775–8782 (2020)

- [20] Kezilebieke, S., Huda, M.N., Vaño, V., Aapro, M., Ganguli, S.C., Silveira, O.J., Głodzik, S., Foster, A.S., Ojanen, T., Liljeroth, P.: Topological superconductivity in a van der Waals heterostructure. *Nature* **588**(7838), 424–428 (2020)
- [21] Fan, P., Yang, F., Qian, G., Chen, H., Zhang, Y.-Y., Li, G., Huang, Z., Xing, Y., Kong, L., Liu, W., *et al.*: Observation of magnetic adatom-induced majorana vortex and its hybridization with field-induced Majorana vortex in an iron-based superconductor. *Nature Communications* **12**(1), 1348 (2021)
- [22] Fu, L., Kane, C.L.: Superconducting proximity effect and Majorana fermions at the surface of a topological insulator. *Physical Review Letters* **100**(9), 096407 (2008)
- [23] Alicea, J., Oreg, Y., Refael, G., Von Oppen, F., Fisher, M.P.: Non-Abelian statistics and topological quantum information processing in 1d wire networks. *Nature Physics* **7**(5), 412–417 (2011)
- [24] Pikulin, D.I., Heck, B., Karzig, T., Martinez, E.A., Nijholt, B., Laeven, T., Winkler, G.W., Watson, J.D., Heedt, S., Temurhan, M., *et al.*: Protocol to identify a topological superconducting phase in a three-terminal device. arXiv preprint arXiv:2103.12217 (2021)
- [25] Zhou, T., Dartiailh, M.C., Sardashti, K., Han, J.E., Matos-Abiague, A., Shabani, J., Žutić, I.: Fusion of Majorana bound states with mini-gate control in two-dimensional systems. *Nature Communications* **13**(1), 1738 (2022)
- [26] Fang, C., Gilbert, M.J., Bernevig, B.A.: New class of topological superconductors protected by magnetic group symmetries. *Physical Review Letters* **112**, 106401 (2014) <https://doi.org/10.1103/PhysRevLett.112.106401>
- [27] Liu, X.-J., He, J.J., Law, K.T.: Demonstrating lattice symmetry protection in topological crystalline superconductors. *Physical Review B* **90**(23), 235141 (2014)
- [28] Hsieh, T.H., Lin, H., Liu, J., Duan, W., Bansil, A., Fu, L.: Topological crystalline insulators in the SnTe material class. *Nature Communications* **3**(1), 1–7 (2012)
- [29] Tanaka, Y., Ren, Z., Sato, T., Nakayama, K., Souma, S., Takahashi, T., Segawa, K., Ando, Y.: Experimental realization of a topological crystalline insulator in SnTe. *Nature Physics* **8**(11), 800–803 (2012)
- [30] Liu, J., Duan, W., Fu, L.: Two types of surface states in topological crystalline insulators. *Physical Review B* **88**(24), 241303 (2013)
- [31] Wang, Y.J., Tsai, W.-F., Lin, H., Xu, S.-Y., Neupane, M., Hasan, M., Bansil, A.: Nontrivial spin texture of the coaxial dirac cones on the surface of topological

- crystalline insulator SnTe. *Physical Review B* **87**(23), 235317 (2013)
- [32] Wang, J., Wang, N., Huang, H., Duan, W.: Electronic properties of SnTe-class topological crystalline insulator materials. *Chinese Physics B* **25**(11), 117313 (2016)
- [33] Klett, R., Schönle, J., Becker, A., Dyck, D., Borisov, K., Rott, K., Ramermann, D., Büker, B., Hasenhoff, J., Krieff, J., *et al.*: Proximity-induced superconductivity and quantum interference in topological crystalline insulator SnTe thin-film devices. *Nano Letters* **18**(2), 1264–1268 (2018)
- [34] Trimble, C., Wei, M., Yuan, N., Kalantre, S., Liu, P., Han, H.-J., Han, M.-G., Zhu, Y., Cha, J., Fu, L., *et al.*: Josephson detection of time-reversal symmetry broken superconductivity in SnTe nanowires. *npj Quantum Materials* **6**(1), 61 (2021)
- [35] Rachmilowitz, B., Zhao, H., Li, H., LaFleur, A., Schneeloch, J., Zhong, R., Gu, G., Zeljkovic, I.: Proximity-induced superconductivity in a topological crystalline insulator. *Physical Review B* **100**(24), 241402 (2019)
- [36] Yang, H., Li, Y.-Y., Liu, T.-T., Xue, H.-Y., Guan, D.-D., Wang, S.-Y., Zheng, H., Liu, C.-H., Fu, L., Jia, J.-F.: Superconductivity of topological surface states and strong proximity effect in $\text{Sn}_{1-x}\text{Pb}_x\text{Te}$ -Pb heterostructures. *Advanced Materials* **31**(52), 1905582 (2019)
- [37] Yang, H., Li, Y.-Y., Liu, T.-T., Guan, D.-D., Wang, S.-Y., Zheng, H., Liu, C., Fu, L., Jia, J.-F.: Multiple in-gap states induced by topological surface states in the superconducting topological crystalline insulator heterostructure $\text{Sn}_{1-x}\text{Pb}_x\text{Te}$ – Pb. *Physical Review Letters* **125**(13), 136802 (2020)
- [38] Liu, T., Yi, Z., Xie, B., Zheng, W., Guan, D., Wang, S., Zheng, H., Liu, C., Yang, H., Li, Y., *et al.*: Fermi level tuning in $\text{Sn}_{1-x}\text{Pb}_x\text{Te}/\text{Pb}$ heterostructure via changing interface roughness. *Science China Physics, Mechanics & Astronomy* **67**(8), 286811 (2024)
- [39] Hulm, J., Jones, C., Deis, D., Fairbank, H., Lawless, P.: Superconducting interactions in Tin Telluride. *Physical Review* **169**(2), 388 (1968)
- [40] Hein, R., Meijer, P.: Critical magnetic fields of superconducting SnTe. *Physical Review* **179**(2), 497 (1969)
- [41] Erickson, A., Chu, J.-H., Toney, M., Geballe, T., Fisher, I.: Enhanced superconducting pairing interaction in indium-doped tin telluride. *Physical Review B* **79**(2), 024520 (2009)
- [42] Balakrishnan, G., Bawden, L., Cavendish, S., Lees, M.R.: Superconducting properties of the in-substituted topological crystalline insulator SnTe. *Physical Review B* **87**(14), 140507 (2013)

- [43] Zhong, R., Schneeloch, J., Shi, X., Xu, Z., Zhang, C., Tranquada, J., Li, Q., Gu, G.: Optimizing the superconducting transition temperature and upper critical field of $\text{Sn}_{1-x}\text{In}_x\text{Te}$. *Physical Review B* **88**(2), 020505 (2013)
- [44] Sato, T., Tanaka, Y., Nakayama, K., Souma, S., Takahashi, T., Sasaki, S., Ren, Z., Taskin, A., Segawa, K., Ando, Y.: Fermiology of the strongly spin-orbit coupled superconductor $\text{Sn}_{1-x}\text{In}_x\text{Te}$: Implications for topological superconductivity. *Physical Review Letters* **110**(20), 206804 (2013)
- [45] Maurya, V., Srivastava, P., Patnaik, S., *et al.*: Superconducting properties of indium-doped topological crystalline insulator SnTe. *Europhysics Letters* **108**(3), 37010 (2014)
- [46] Maeda, S., Hirose, R., Matano, K., Novak, M., Ando, Y., Zheng, G.-q.: Spin-singlet superconductivity in the doped topological crystalline insulator $\text{Sn}_{0.96}\text{In}_{0.04}\text{Te}$. *Physical Review B* **96**(10), 104502 (2017)
- [47] Smylie, M., Claus, H., Kwok, W.-K., Loudon, E., Eskildsen, M., Sefat, A., Zhong, R., Schneeloch, J., Gu, G., Bokari, E., *et al.*: Superconductivity, pairing symmetry, and disorder in the doped topological insulator $\text{Sn}_{1-x}\text{In}_x\text{Te}$ for $x \leq 0.10$. *Physical Review B* **97**(2), 024511 (2018)
- [48] Bliesener, A., Feng, J., Taskin, A., Ando, Y.: Superconductivity in $\text{Sn}_{1-x}\text{In}_x\text{Te}$ thin films grown by molecular beam epitaxy. *Physical Review Materials* **3**(10), 101201 (2019)
- [49] Nomoto, T., Kawamura, M., Koretsune, T., Arita, R., Machida, T., Hanaguri, T., Kriener, M., Taguchi, Y., Tokura, Y.: Microscopic characterization of the superconducting gap function in $\text{Sn}_{1-x}\text{In}_x\text{Te}$. *Physical Review B* **101**(1), 014505 (2020)
- [50] Smylie, M., Kobayashi, K., Takahashi, T., Chaparro, C., Snezhko, A., Kwok, W.-K., Welp, U.: Nodeless superconducting gap in the candidate topological superconductor $\text{Sn}_{1-x}\text{In}_x\text{Te}$ for $x = 0.7$. *Physical Review B* **101**(9), 094513 (2020)
- [51] Smylie, M., Kobayashi, K., Dans, J., Hebbeker, H., Chapai, R., Kwok, W.-K., Welp, U.: Full superconducting gap in the candidate topological superconductor $\text{In}_{1-x}\text{Pb}_x\text{Te}$ for $x = 0.2$. *Physical Review B* **106**(5), 054503 (2022)
- [52] Tewari, S., Sau, J.D.: Topological invariants for spin-orbit coupled superconductor nanowires. *Physical Review Letters* **109**(15), 150408 (2012)
- [53] Hell, M., Leijnse, M., Flensberg, K.: Two-dimensional platform for networks of Majorana bound states. *Physical Review Letters* **118**(10), 107701 (2017)
- [54] Sun, H.-H., Jia, J.-F.: Detection of Majorana zero mode in the vortex. *npj*

- [55] Hosur, P., Ghaemi, P., Mong, R.S., Vishwanath, A.: Majorana modes at the ends of superconductor vortices in doped topological insulators. *Physical Review Letters* **107**(9), 097001 (2011)
- [56] Chiu, C.-K., Gilbert, M.J., Hughes, T.L.: Vortex lines in topological insulator-superconductor heterostructures. *Physical Review B* **84**(14), 144507 (2011)
- [57] Caroli, C., De Gennes, P., Matricon, J.: Bound fermion states on a vortex line in a type ii superconductor. *Physics Letters* **9**(4), 307–309 (1964)
- [58] Volovik, G.: Fermion zero modes on vortices in chiral superconductors. *Journal of Experimental and Theoretical Physics Letters* **70**(9), 609–614 (1999)
- [59] Khaymovich, I., Kopnin, N., Mel’Nikov, A., Shereshevskii, I.: Vortex core states in superconducting graphene. *Physical Review B* **79**(22), 224506 (2009)
- [60] Hess, H., Robinson, R., Waszczak, J.: Vortex-core structure observed with a scanning tunneling microscope. *Physical Review Letters* **64**(22), 2711 (1990)
- [61] Li, Z.-Z., Zhang, F.-C., Wang, Q.-H.: Majorana modes in a topological insulator/s-wave superconductor heterostructure. *Scientific Reports* **4**(1), 1–6 (2014)
- [62] Kawakami, T., Hu, X.: Evolution of density of states and a spin-resolved checkerboard-type pattern associated with the Majorana bound state. *Physical Review Letters* **115**(17), 177001 (2015)
- [63] Yan, Z., Wu, Z., Huang, W.: Vortex end Majorana zero modes in superconducting Dirac and Weyl semimetals. *Physical Review Letters* **124**(25), 257001 (2020)
- [64] Kobayashi, S., Furusaki, A.: Double Majorana vortex zero modes in superconducting topological crystalline insulators with surface rotation anomaly. *Physical Review B* **102**(18), 180505 (2020)
- [65] Kobayashi, S., Sumita, S., Hirayama, M., Furusaki, A.: Crystal-symmetry-protected gapless vortex-line phases in superconducting Dirac semimetals. *Physical Review B* **107**(21), 214518 (2023)
- [66] Hu, L.-H., Wu, X., Liu, C.-X., Zhang, R.-X.: Competing vortex topologies in iron-based superconductors. *Physical Review Letters* **129**(27), 277001 (2022)
- [67] Schnyder, A.P., Ryu, S., Furusaki, A., Ludwig, A.W.: Classification of topological insulators and superconductors in three spatial dimensions. *Physical Review B* **78**(19), 195125 (2008)
- [68] Chiu, C.-K., Teo, J.C., Schnyder, A.P., Ryu, S.: Classification of topological

- quantum matter with symmetries. *Reviews of Modern Physics* **88**(3), 035005 (2016)
- [69] Weiße, A., Wellein, G., Alvermann, A., Fehske, H.: The kernel polynomial method. *Reviews of modern physics* **78**(1), 275 (2006)
- [70] Nagai, Y., Ota, Y., Machida, M.: Efficient numerical self-consistent mean-field approach for fermionic many-body systems by polynomial expansion on spectral density. *Journal of the Physical Society of Japan* **81**(2), 024710 (2012)
- [71] Liu, T., Wan, C.Y., Yang, H., Zhao, Y., Xie, B., Zheng, W., Yi, Z., Guan, D., Wang, S., Zheng, H., et al.: Signatures of hybridization of multiple majorana zero modes in a vortex **633**, 71 (2024)
- [72] Shore, J.D., Huang, M., Dorsey, A.T., Sethna, J.P.: Density of states in a vortex core and the zero-bias tunneling peak. *Physical review letters* **62**(26), 3089 (1989)
- [73] Gygi, F., Schlüter, M.: Self-consistent electronic structure of a vortex line in a type-II superconductor. *Physical Review B* **43**(10), 7609 (1991)
- [74] Datta, S.: *Electronic Transport in Mesoscopic Systems*. Cambridge university press, Cambridge (1997)
- [75] Nagai, Y., Nakai, N., Machida, M.: Direct numerical demonstration of sign-preserving quasiparticle interference via an impurity inside a vortex core in an unconventional superconductor. *Physical Review B* **85**(9), 092505 (2012)
- [76] Smith, E.D., Tanaka, K., Nagai, Y.: Manifestation of chirality in the vortex lattice in a two-dimensional topological superconductor. *Physical Review B* **94**(6), 064515 (2016)
- [77] Berthod, C.: Vortex spectroscopy in the vortex glass: A real-space numerical approach. *Physical Review B* **94**(18), 184510 (2016)
- [78] Galvis, J., Herrera, E., Berthod, C., Vieira, S., Guillamón, I., Suderow, H.: Tilted vortex cores and superconducting gap anisotropy in 2H-NbSe₂. *Communications Physics* **1**(1), 1–9 (2018)
- [79] Berthod, C.: Signatures of nodeless multiband superconductivity and particle-hole crossover in the vortex cores of FeTe_{0.55}Se_{0.45}. *Physical Review B* **98**(14), 144519 (2018)
- [80] Mitchell, D., Wallis, R.: Theoretical energy-band parameters for the lead salts. *Physical Review* **151**(2), 581 (1966)
- [81] Fulga, I., Avraham, N., Beidenkopf, H., Stern, A.: Coupled-layer description of topological crystalline insulators. *Physical Review B* **94**(12), 125405 (2016)

- [82] Zhu, Z., Papaj, M., Nie, X.-A., Xu, H.-K., Gu, Y.-S., Yang, X., Guan, D., Wang, S., Li, Y., Liu, C., *et al.*: Discovery of segmented fermi surface induced by Cooper pair momentum. *Science* **374**(6573), 1381–1385 (2021)
- [83] Pan, X.-H., Chen, L., Liu, D.E., Zhang, F.-C., Liu, X.: Majorana zero modes induced by the Meissner effect at small magnetic field. *Physical Review Letters* **132**(3), 036602 (2024)
- [84] Qin, S., Hu, L., Le, C., Zeng, J., Zhang, F.-c., Fang, C., Hu, J.: Quasi-1d topological nodal vortex line phase in doped superconducting 3d dirac semimetals. *Physical Review Letters* **123**(2), 027003 (2019)
- [85] Jackiw, R., Rossi, P.: Zero modes of the vortex-fermion system. *Nuclear Physics B* **190**(4), 681–691 (1981)
- [86] Sancho, M.L., Sancho, J.L., Sancho, J.L., Rubio, J.: Highly convergent schemes for the calculation of bulk and surface Green functions. *Journal of Physics F: Metal Physics* **15**(4), 851 (1985)
- [87] Xiong, Y., Yamakage, A., Kobayashi, S., Sato, M., Tanaka, Y.: Anisotropic magnetic responses of topological crystalline superconductors. *Crystals* **7**(2), 58 (2017)
- [88] Sato, M., Fujimoto, S.: Majorana fermions and topology in superconductors. *Journal of the Physical Society of Japan* **85**(7), 072001 (2016)